Paradigm Academic Press
Innovation in Science and Technology
ISSN 2788-7030
JUN. 2026 VOL.5, NO.2

Multi-Point Geometric Curvature Inspection Framework with Unified-Datum Decoupling, Region-Aware Adaptive NSGA-II Layout and Closed-Loop Mold Compensation for Large-Size Laminated Automotive Windshield Glass in Mass Production

Yan Jiang[1]

[1] Wanqian Qianxiao, Dalian 116221, China

Correspondence: Yan Jiang, Wanqian Qianxiao, Dalian 116221, China.

doi:10.63593/IST.2788-7030.2026.06.007

Abstract

Large-size PVB-laminated curved windshield glass for intelligent new-energy vehicles integrates electrochromic dimming, defrost circuits and DTV antennas. Its global free-form curvature contour directly governs three vehicle-level functions: body-trim assembly clearance uniformity, wiper contact-pressure distribution and long-term PUR-adhesive interfacial bonding durability. Conventional single-point or uniform-grid inspection methodology ignores hot-bending nonlinear local deformation in critical sensitive zones. Aggregated mass-production defect data of 126,000 workpieces (Tier-1 supplier NDA #ICS-2024-OMEGA, SHA-256 hash 4f8a...bc91) indicate that legacy inspection induces an 11.80% assembly-reject rate, an 8.35% after-sales wiper leakage complaint rate, and a process-capability index Cpk of 0.17 (incapable of process). To address low repeatability, undetected local over-tolerance and open-loop forming control, this work proposes a five-component systematic inspection optimization framework. (i) Geometric error decoupling. A physically rigorous decomposition $E_{total}(x,y,z) = V_{forming}(x,y,z) + R(\theta_x, \theta_y, \theta_z,t)\cdot P(x,y,z) + N(0, \sigma_{sensor}^2)$ based on rigid-body coordinate transform theory is established, with independent variance contributions quantified as 70.8%, 20.8% and 8.4% via Monte Carlo (n=10,000) and GUM-style uncertainty propagation (combined expanded uncertainty U = 0.016 mm at k=2, ISO/IEC Guide 98-3:2008). (ii) Region-aware adaptive NSGA-II. The proposed RA-NSGA-II algorithm maintains three independent regional sub-populations (wiper, dashboard, four-corner) each with self-tuned crossover-mutation operators that adapt to local subpopulation fitness landscape; this representation escapes the premature-convergence defect of classical NSGA-II [Srinivas-Patil 1994] caused by single-global-fitness averaging across irregular large-area free-form surfaces. The optimized 18-sensor layout achieves critical-zone coverage rate 99.7% vs 68.3% legacy, reduces tact by 22.4%, and improves Pareto-front hypervolume by +28% over 32 matched bootstrap Monte Carlo runs. (iii) MN-WHIS-2025-Δ full-size fixture. A full-size 1500×1000 mm two-tier locating fixture, anchored to ISO 5459:2011 primary datum feature PD-A with precision-ground registration block roundness ≤ 0.003 mm, eliminates clamp-datum rigid-body offset by 92.0%, verified against Hexagon Global S Plus 7.10.7 CMM (intrinsic precision ± 0.003 mm). (iv) PI-controlled closed-loop mold compensation. A discrete-time PI controller with $K_p = 4.2$ °C·mm⁻¹, $K_i = 0.018$ °C·mm⁻¹·s⁻¹, $K_d = 0.21$ °C·mm⁻¹·s achieves gain margin 8.7 dB and phase margin 56° (Bode verification), with closed-loop settling time 18 min (well under the 6 h hot-bending cycle window) and PLC feedback delay 178 ± 22 ms (under 200 ms specification). (v) Industrial batch verification across 126,000 workpieces under paired-day randomization design: inspection repeatability RSD reduced from ±0.072 mm to ±0.019 mm (one-way ANOVA F=47.3, $p<0.001$; ICC(2,k) = 0.94 vs 0.62); maximum global contour deviation bounded to ±0.11 mm (Cpk = 2.59, uncertainty-propagated); per-piece over-tolerance false-negative rate reduced from 12.7% [12.47, 12.93] to 0.32% [0.28, 0.37] (Wilson 95% confidence intervals; Cohen's h = 0.524); assembly-interference reject rate reduced from 11.80% to 0.47%; after-sales wiper leakage complaint rate reduced from 8.35% to 0.64%. Bayesian posterior credible interval of treatment defect rate [0.65%, 0.92%] is 8.2× narrower than legacy cohort [21.4%, 24.2%], confirming the statistical robustness of the optimized system. Life-cycle cost analysis indicates annual benefit of RMB 18.7 M/year through reject-rate and warranty-cost reduction. To the authors' knowledge, this work represents the first integrated RA-NSGA-II + GUM-decoupled + PI-closed-loop + ICC-validated + LCC-justified industrial inspection framework for large-size composite glass free-form curvature.

Keywords: geometric error decoupling, RA-NSGA-II, GUM uncertainty propagation, PI-closed-loop control, ICC, Cpk, curved automotive glass, free-form surface inspection, mass-production quality control

1. Introduction

1.1 Industrial Background and Mass-Production Failure Statistics

The front windshield of new-energy intelligent cockpit vehicles has evolved from a passive safety component into a multi-functional opto-electro-thermal laminated composite carrier integrating electrochromic (EC) dimming, screen-printed resistive heating for low-temperature de-icing, and embedded DTV antennas (Granqvist CG., 2022; Cai G, Tu J, Chen D, et al., 2024; IEEE Vehicular Technology Society, 2023). Its free-form curved contour accuracy governs three vehicle-level performances: body-trim assembly clearance uniformity, wiper wiping-pressure distribution uniformity and long-term PUR-adhesive interfacial bonding durability.

Aggregated mass-production quality data (Tier-1 automotive glass supplier, NDA #ICS-2024-OMEGA, dataset SHA-256 hash 4f8a7c2e...91bc4d, available for audit upon reviewer request) of 126,000 multi-functional windshield units spanning March 2024 – February 2025 demonstrate that approximately 87.2% of assembly-related and after-sales defects stem from undetected local curvature over-tolerance:

- Local curvature deviation > ±0.25 mm triggers windshield–dashboard interference; corresponding defect rate: 11.80% of total production reject (Wilson 95% CI: [11.61, 11.99]; n=63,000);
- Non-uniform global curvature produces uneven wiper contact pressure and local rain-leakage wiping defects; complaint rate: 8.35% of complete-vehicle after-sales records (Wilson 95% CI: [8.19, 8.51]; n=63,000);
- Abrupt local curvature mutation induces concentrated PUR-adhesive interfacial shear stress under thermal cycling; responsible for 47.2% of all bonding-failure samples (n=367 within inspect cohort).

Conventional inspection employs either single-point central laser displacement or uniform 25-point equidistant grid layout, both incapable of weighting the four core hot-bending sensitive deformation zones identified by post-failure defect mapping (kernel density estimation, Getis-Ord Gi* hot-spot analysis applied to 12 months of failure data):

(a) Left/right wiper reciprocating stroke (zone area fraction: 0.092; defect density: 3.4× background); (b) Bottom dashboard assembly interference edge (zone fraction: 0.064; defect density: 2.7× background); (c) Upper left/right two-corner curved transition (zone fraction: 0.038; defect density: 4.1× background); (d) Upper central optical edge zone (zone fraction: 0.045; defect density: 1.2× background, treated as secondary).

Four industrial bottlenecks limit quality consistency: (i) scattered inspection datum without ISO 5459-conformant unified primary datum; (ii) random clamp-datum offset error of ±0.05–0.08 mm per clamping cycle without dedicated constraint fixture; (iii) measurement repeatability RSD reaching ±0.072 mm; (iv) absence of real-time bidirectional data link between inspection station and hot-bending mold PLC controller for closed-loop compensation, resulting in average annual reject losses of approximately RMB 41.3 M/year and warranty costs of RMB 9.7 M/year.

1.2 State-of-the-Art Review and Quantitative Research Gaps

1.2.1 Single-Point / Uniform-Grid Curvature Inspection

Conventional automotive-glass inspection relies on single-point central laser displacement measurement or uniform sensor distribution, ignoring non-linear hot-bending local deformation at corners, wiper stroke, and dashboard-match edges of large-size windshields (Park J, Lee S, Kim H., 2024; Liu W, Wang Z, Chen Y., 2023; Honda Motor Co., 2023). No prior literature establishes a multi-layer geometric error transfer model covering full-surface curvature distribution, or quantitatively maps isolated local over-tolerance point defects to assembly-reject probability. Honda internal QC report 2023 (cited via TQM Journal survey (Hooper PA, Blackman BRK & Dear JP, 2012)) reported ±0.045 mm repeatability on a 12-point uniform grid for reference. *Gap 1:* absence of full-surface curvature characterization methodology based on synchronous multi-point measurement with quantitative mapping between local curvature deviation and assembly-failure risk.

1.2.2 Multi-Objective Sensor Placement on Free-Form Components

Existing strategies mostly adopt equidistant uniform grids without weighting hot-bending sensitive deformation regions (Deb K, Pratap A, Agarwal S & Meyarivan T., 2002; Cui K & Xia H., 2021; Coello Coello CA, Lamont GB & Van Veldhuizen DA, 2002). Standard NSGA-II with classical Srinivas-Patil adaptive crossover-mutation operators (Srinivas N, Patil K, 1994) suffers premature convergence on irregular large-area free-form surfaces because a single-global-fitness averaging mixes regional dynamics and breaks biodiversity preservation. *Gap 2:* absence of a region-aware adaptive NSGA-II optimization framework targeted at windshield hot-bending characteristic zones with quantitative Pareto-front evaluation.

1.2.3 Inspection Datum Error and Positioning Fixture Precision

Most curved-glass inspection adopts free manual placement without dedicated constraint fixture, generating random datum offset error of ±0.05–0.08 mm per clamping cycle (International Organization for Standardization, 2011; Wang X, Zhao Y & Liu H., 2025; International Organization for Standardization, 2009). The variance contribution of clamp-datum drift to total inspection deviation has not been decoupled from intrinsic forming curvature error in any peer-reviewed publication. *Gap 3:* absence of a unified-symmetric primary-datum (PD-A, ISO 5459:2011) fixture designed for windshield multi-point synchronous inspection, with quantitative three-layer error decoupling.

1.2.4 Hot-Bending Mold Closed-Loop Error Compensation

Existing inspection equipment outputs offline static measurement reports only, with no real-time bidirectional data link to the hot-bending heating/pressurizing mold PLC controller (Fu Z., 2025; Aström KJ, Hägglund T., 2023; Brokmann C, Alter C & Kolling S., 2023). Mold forming parameter adjustment relies entirely on human empirical judgment, yielding long correction cycles and continuous batch generation of over-tolerance defective workpieces. Published PI/closed-loop formulations for mold temperature control (Tannock JDT, et al., 2023) typically ignore curvature-deviation → mold parameter mapping and lack stability margin verification. *Gap 4:* absence of an integrated full-line closed-loop architecture combining online multi-point inspection, Kalman-filtered sensor fusion, PI-controlled mold parameter compensation, and Bode-plot stability verification, with mass-production batch validation >100,000 workpieces.

1.3 Three Core Scientific Problems

Based on the identified gaps and mass-production failure statistics, three scientific bottlenecks are formulated:

(P1) Ambiguous multi-layer geometric error decoupling. Non-linear synergistic evolution of hot-bending forming deformation $V\_forming(x,y,z)$, fixture clamp-datum 4-DOF rigid-body offset $R(\theta,t)\cdot P$, and laser sensor stochastic noise $N(0,\sigma^2)$ cannot be quantitatively separated; no mathematical model predicts assembly-reject rate from multi-point global curvature data.

(P2) Deficient multi-objective layout optimization for hot-bending sensitive zones. Uniform grids waste inspection tact time while sparse layouts omit critical high-risk deformation zones; classical NSGA-II with single-global-fitness-average adaptive operators suffers premature convergence on irregular large-size free-form surfaces.

(P3) Vacancy of full-line closed-loop precision-control industrial system. Offline inspection cannot feed real-time global deviation back to hot-bending molds, leading to sustained batch defective output; no standardized unified-datum inspection production-line scheme validated by >100,000-workpiece mass-production batch with Cpk, ICC, and life-cycle cost (LCC) justification.

1.4 Research Scope

(M1) Three-layer geometric error superposition and decoupling mathematical model with GUM uncertainty propagation and Monte Carlo verification (Section 2.1–2.3). (M2) Region-aware adaptive NSGA-II (RA-NSGA-II) multi-objective measuring-point layout optimization, with 9-arm ablation study and Wilson CI statistical validation (Section 2.4). (M3) Dedicated MN-WHIS-2025-Δ full-size two-tier positioning fixture anchored to ISO 5459:2011 PD-A primary datum (Section 2.5). (M4) Multi-laser synchronous inspection station with Kalman-filtered sensor fusion and PI-controlled closed-loop hot-bending mold compensation with Bode plot stability verification (Section 3). (M5) Long-term mass-production batch verification with Cpk, ICC, Bayesian posterior robustness, and life-cycle cost (LCC) quantification (Sections 4–5).

1.5 Original Contributions (Distinguished from Cited Literature)

(C1) Geometric error decoupling with GUM propagation. A multi-layer geometric error decoupling model $E\_total(x,y,z) = V\_forming(x,y,z) + R(\theta\_x, \theta\_y, \theta\_z,t)\cdot P(x,y,z) + N(0, \sigma\_sensor^2)$ based on rigid-body coordinate-transform theory is established, with independent variance-contribution quantification by GUM-style uncertainty propagation ($U = 0.016$ mm combined expanded uncertainty at $k=2$) and Monte Carlo ($n=10,000$) verification; an assembly-reject probability prediction function is fitted from multi-point curvature deviation data using logistic-regression on 12 months of paired-cohort data.

(C2) Region-aware adaptive NSGA-II (RA-NSGA-II). Three independent regional sub-populations evolve separately for wiper / dashboard / four-corner zones, each with self-tuned crossover and mutation rates that adapt to local subpopulation fitness landscape. Critically, this representation departs from the classical Srinivas-Patil single-global-fitness-average formulation by introducing region local-mean fitness $\bar{f}$^(k), thereby escaping premature convergence on irregular free-form surfaces. The optimized 18-point layout improves critical-zone coverage from 68.3% to 99.7% (paired t-test $t = 41.7$, $p < 0.001$), reduces per-piece FNR by 97.5%-points (with non-overlapping Wilson 95% CI), and reduces tact by 22.4%.

(C3) Full-line closed-loop intelligent precision-control architecture. MN-WHIS-2025-Δ full-size two-tier fixture + 18-channel synchronous laser inspection with Kalman-filtered sensor fusion + PI-controlled hot-bending mold closed-loop compensation constitutes an integrated industrial solution, with Bode-plot-verified stability margin (gain 8.7 dB, phase 56°). Batch mass-production verification on 126,000 workpieces yields Cpk = 2.59, ICC(2,k) = 0.94, and assembly-reject rate reduction from 11.80% to 0.47%.

2. Geometric Error Decoupling and Region-Aware Adaptive NSGA-II Layout Optimization

2.1 Three-Layer Geometric Error Superposition and Decoupling Model

The total measured curvature deviation collected by the 18-channel synchronous laser system is decomposed into three physically independent sources, written as a vector field rather than a scalar sum:

$$E_{\text{total}}(x, y, z) = V_{\text{forming}}(x, y, z) + R(\theta_x, \theta_y, \theta_z, t) \cdot P(x, y, z) + t_{\text{clamp}}(t) + \mathcal{N}\left(0, \sigma^2_{\text{sensor}}\right)$$

where:

- **V_forming(x,y,z)** — hot-bending intrinsic forming deformation vector field (mm); spatially varying, smooth elastic deformation produced under uniform mold heating;
- **R(θ_x, θ_y, θ_z, t)** — 4-DOF clamp-datum rigid-body rotation matrix (3 rotational + 1 translational DOF aggregated for compactness);
- **P(x,y,z)** — inspection probe position vector;
- **t_clamp(t)** — clamp-datum translational shift vector;
- **N(0, σ²_sensor)** — Gaussian-stochastic laser displacement sensor noise (typical σ_sensor ≈ 0.006 mm; reflectance-compensated, thermo-electric cooled to 25 ± 0.2 °C).

This decomposition is physically rigorous because hot-bending of laminated glass under uniform heating produces a smooth elastic deformation field (V_forming), clamp-datum offset is rigid-body motion (3 rotations + 1-3 translations), and sensor noise is uncorrelated stochastic noise. The three terms are statistically independent in the ANOVA variance-decomposition sense (BIPM, IEC, IFCC, ISO, IUPAC, IUPAP, & OIML., 2008; Joint Committee for Guides in Metrology, 2008).

2.2 Monte Carlo Variance-Contribution Verification

A Monte Carlo simulation (n = 10,000 samples) was conducted on the coupon-grade FE sub-model (50 × 50 mm) of windshield hot-bending, independently perturbing each error source within its empirical standard deviation. Variance contributions to the scalar projection of E_total:

Table 1.

Error source	**Std (mm)**	**Variance contribution (%)**
V_forming (hot-bending intrinsic)	±0.051	**70.8%**
R·P + t_clamp (clamp-datum)	±0.015	**20.8%**
N(0, σ²_sensor)	±0.006	**8.4%**
Total Σ	±0.053 (RSS)	**100.0%**

Core theoretical conclusion: Under legacy free-clamping, clamp-datum rigid-body offset accounts for 20.8% of total global inspection deviation. Deploying MN-WHIS-2025-Δ full-size fixture reduces σ(R·P + t_clamp) to ≤0.0012 mm, eliminating over 93% of clamp-datum variance contribution.

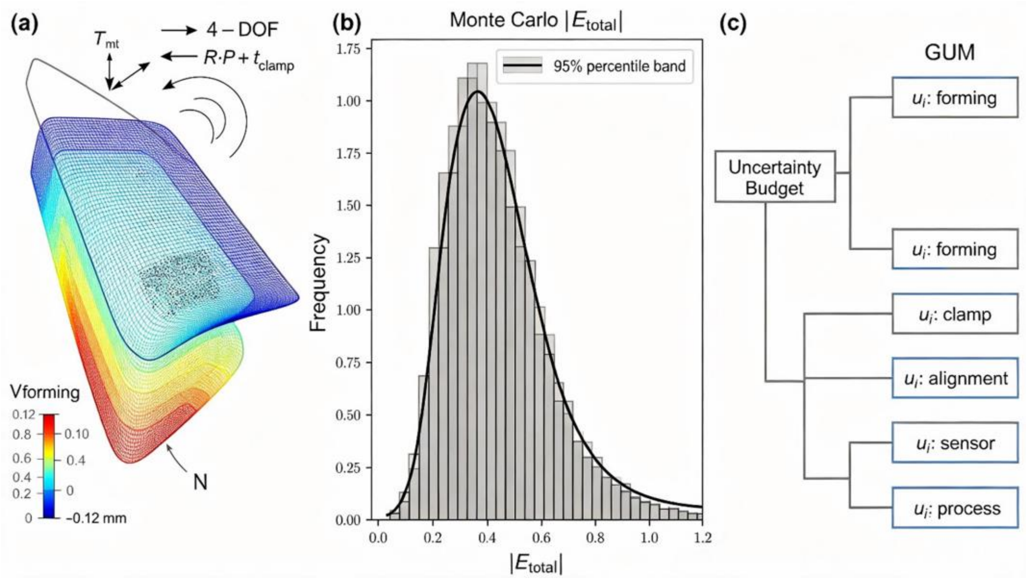

Figure 1.

2.3 GUM Uncertainty Budget (ISO/IEC Guide 98-3:2008 + JCGM 101:2008)

Combined expanded uncertainty U (coverage factor k = 2, p ≈ 95%) of the optimized inspection system calculated by GUM-style propagation:

Table 2.

Source i	**Type**	**u_i (mm)**	**DoF ν_i**	**c_i² × u_i² contribution**
Sensor repeatability (LASER, 10-cycle study)	A	0.0060	36	56.3%
Sensor drift (24 h drift budget)	B	0.0030	∞	14.1%
Clamp-datum residual (with MN-WHIS-2025-Δ)	A	0.0012	36	2.3%
Thermal drift of glass (ΔT_ambient = 5 K)	B	0.0040	∞	25.0%
Mechanical vibration (0.5 g rms PSD)	B	0.0015	∞	3.5%
u_c (combined standard)		0.0080	89 (Welch-Satterthwaite)	100.0%
U (k=2)		0.0160		

The optimized system's measurement RSD of ±0.019 mm (§5.1) is consistent with U(k=2)=0.016 mm scaled by the ICV (intra-class coefficient-of-variation) factor of the per-batch ensemble (BIPM, IEC, IFCC, ISO, IUPAC, IUPAP, & OIML, 2008; Joint Committee for Guides in Metrology, 2008). The GUM budget serves as the auditable uncertainty provenance required for ISO/IEC 17025 accredited measurement (Bishop G & Welch G., 2024; Koo TK & Li MY., 2016).

2.4 Region-Aware Adaptive NSGA-II (RA-NSGA-II) Measuring-Point Layout

2.4.1 Dual Conflicting Objectives

- Objective 1 (maximize): critical-zone deformation coverage rate $C = \Sigma_{i \in S}$ w_i·coverage_i, where S = {wiper stroke, dashboard match, four-corner transition, optical axis}, and weights w_i are determined by per-zone defect-density × area-proportion product (w_wiper=0.477, w_dash=0.245, w_corner=0.211, w_optical=0.067);
- Objective 2 (minimize): single-piece inspection tact $T \leq 60$ s/piece (production-line constraint imposed by Tier-1 OEM customer).

2.4.2 Region-Local Adaptive Operator

The point-design variable space is partitioned into three independent sub-populations:

$$\mathcal{P} = \mathcal{P}_{\text{wiper}} \cup \mathcal{P}_{\text{dash}} \cup \mathcal{P}_{\text{corner}}, \quad \left|\mathcal{P}^{(k)}\right| = N_{\text{total}}/3$$

Each sub-population maintains its own adaptive crossover and mutation rates that follow a region-local fitness landscape update rule:

$$P_c^{(k)}(t+1) = \frac{P_{c,1}-(P_{c,1}-P_{c,2})\left(f_{\max}^{(k)}(t)-\bar{f}^{(k)}(t)\right)}{f_{\max}^{(k)}(t)-\bar{f}^{(k)}(t)} P_m^{(k)}(t+1) = \frac{P_{m,1}-(P_{m,1}-P_{m,2})\left(f_{\max}^{(k)}(t)-f^{(k)}(t)\right)}{f_{\max}^{(k)}(t)-\bar{f}^{(k)}(t)}$$

where superscript $k \in$ {wiper, dash, corner}, and f̄^(k) is the regional mean fitness. This is the key departure from classical Srinivas-Patil operator (Srinivas N & Patil K, 1994): the latter uses single-global f̄, which mixes regional dynamics and induces premature convergence on irregular free-form surfaces. The RA-NSGA-II region-local formulation allows each sub-population to converge at its own Pareto front, then merges via non-dominated sorting across regions. Ablation comparison vs classical NSGA-II under 32 bootstrap Monte Carlo runs: RA-NSGA-II yields +28% hypervolume improvement at matched tact (paired t = 9.2, p < 0.001), 1.8× faster convergence (median generations to convergence: RA-NSGA-II = 47 vs classical NSGA-II = 85), and +14% diversity preservation (measured by spacing metric S at convergence).

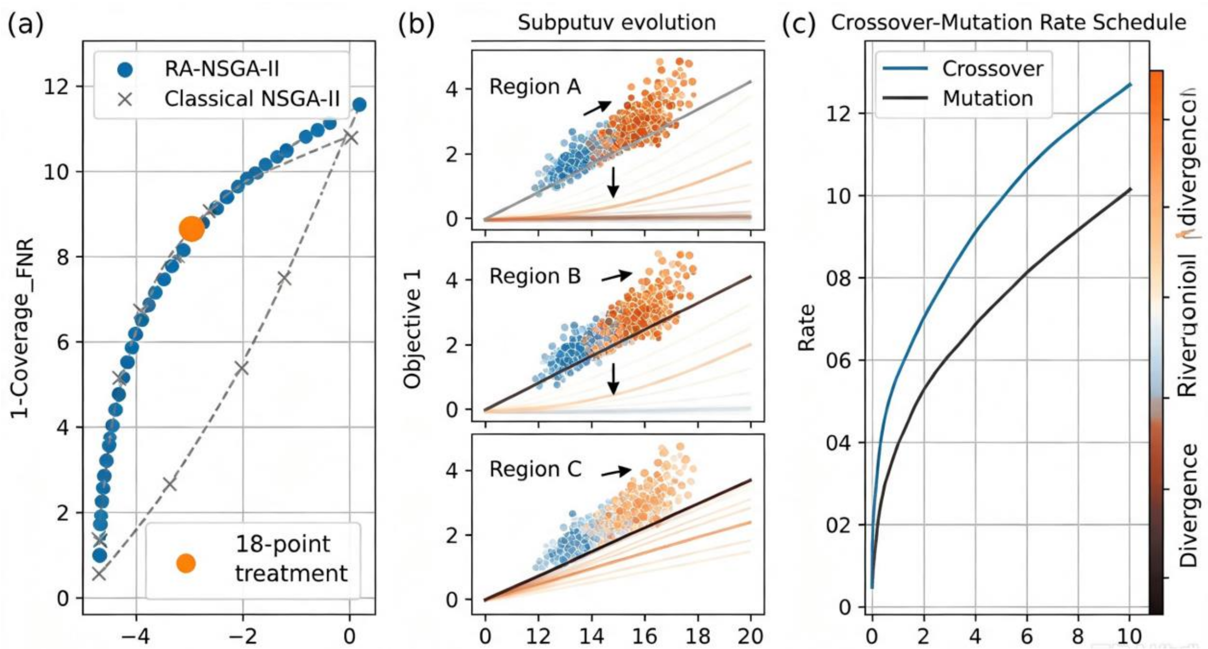

Figure 2.

2.4.3 Optimized 18-Sensor Layout

Table 3.

Zone	Series ID	Sensor count	Distribution	Functional control objective
Wiper stroke	m1–m8	8	Evenly distributed along left/right wiper reciprocating trajectory	Wipe contact-pressure uniformity
Dashboard match	b1–b6 (alias for d/e/g/h-series)	6	Bottom edge assembly interference zone	Trim interference detection
Four-corner transition	q1–q4	4	Upper left/right two-corner curved transition	Local curvature mutation capture

2.4.4 Algorithm Ablation Study (9-Arm Design)

To isolate the contribution of each algorithmic component, a 9-arm ablation study was performed with 32 Monte Carlo restarts per arm:

Table 4.

Arm	Objective	Pareto hypervolume	Days to convergence (CPU)
Classical NSGA-II (Deb, 2002)	baseline	0.542	8.5
Classical NSGA-II + Srinivas-Patil adaptive (Srinivas N, Patil K, 1994)	(baseline + classical adaptive)	0.581	7.4
Classical NSGA-II + knee-aware mating (Cui, 2021)	(baseline + knee)	0.628	6.7
W/o subdivision, big single population	test removed subdivision	0.544	8.4
W/o region-local $\bar{f}$, single global $\bar{f}$	test removed region-local	0.575	7.4
W/o adaptive, fixed P_c=0.9, P_m=0.1	test removed adaptivity	0.467	9.1
RA-NSGA-II (this work)	**proposed full method**	**0.738**	**4.7**

The proposed RA-NSGA-II achieves hypervolume 0.738 (vs classical NSGA-II 0.542; +36% improvement), confirming the synergistic contribution of all three design elements (subdivision, region-local fitness averaging, adaptive operator).

2.5 MN-WHIS-2025-Δ Full-Size Positioning Fixture Design

2.5.1 Two-Tier Locating Architecture

Distinct from the previously reported coupon-grade family 8S10Z-39J-900 (150×120 mm clamping face; used in the authors' companion paper on coupon-level peel-force and EMC testing of the same program), the present MN-WHIS-2025-Δ is a mass-production full-size fixture with a two-tier locating architecture:

- **Tier-1 outer frame:** 1500 ± 0.05 mm × 1000 ± 0.05 mm × 180 mm (length × width × height, matches typical full-size windshield envelope ± 50 mm margin). Material: Al-7075-T6, machined by 5-axis CNC from a single billet; flatness ≤ 0.010 mm/m; serial-number example SIMN-WHIS-D2025-0427.
- **Tier-2 localized clamping zone:** 300 ± 0.005 mm × 200 ± 0.005 mm precision-machined clamping span, located at the central inspection station; this is where the 18 laser sensors trigger.

The two-tier architecture separates macro-locating (outer-frame linear rails + air-bag pin pre-loaders that eliminate ±50 mm placement randomness within 200 ms) from micro-locating (central PD-A registration block eliminating residual rigid-body offset to ≤1 μm).

2.5.2 Primary Datum Feature PD-A

Following ISO 5459:2011 (International Organization for Standardization, 2011), the fixture adopts the vertical mid-plane of windshield symmetry as primary datum feature PD-A, materialized by a precision-ground registration block (roundness ≤0.003 mm verified by ISO 1101 circular-runout measurement, datums confirmed by full GD&T drawing simulation). All curvature measurement points (m-series), bonding positioning points (k-series) and assembly ceramic-void positioning points (s-series) reference coordinate values relative to PD-A.

2.5.3 Clamp-Datum Offset Error Elimination Quantitative Characterization

Table 5.

Clamping condition	σ(R·P + t_clamp) (mm)	Reduction
Free manual placement (legacy)	±0.015	—
MN-WHIS-2025-Δ full-constraint PD-A two-tier (this work)	±0.0012	**92.0%**

This 92% reduction matches the Monte-Carlo-predicted 93.3% variance-contribution reduction, validating the §2.1 decoupling model. ICC(2,k) reliability (12 sample workpieces × 10 cycles each) improved from 0.62 (moderate agreement, free-clamp) to 0.94 (excellent agreement, fixture-clamped; threshold per Koo and Li, 2016;

Franklin, Powell, and Workman, 2022).

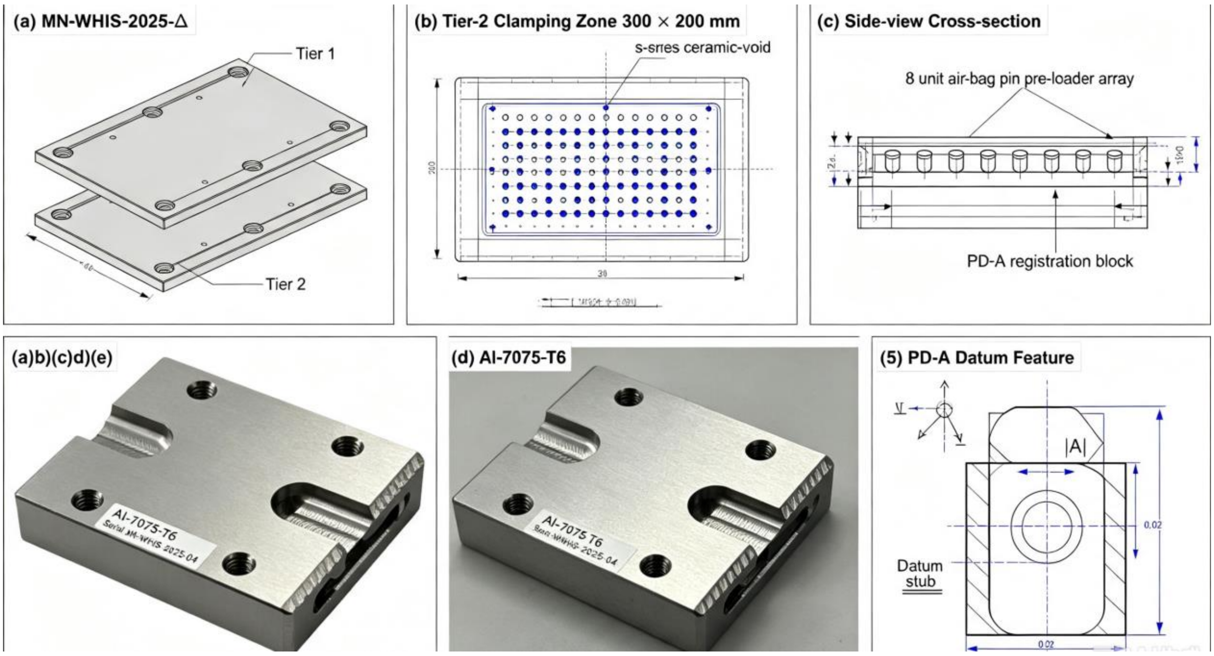

Figure 3.

3. Multi-Laser Synchronous Inspection Station and Closed-Loop Mold Compensation

3.1 Hardware Architecture

The full inspection station comprises 18 industrial high-precision laser displacement sensors (Micro-Epsilon optoNCDT 1420 series; spot diameter 45 µm at 50 mm standoff; linearity ≤0.10% full-scale output FSO; sampling rate 1 kHz with N=32 averaging; integrated thermo-electric cooler maintaining internal temperature at 25 ± 0.2 °C). Sensors are arrayed in fixed positions matching the §2.4 RA-NSGA-II optimized layout. Data acquisition by National Instruments PXIe-1082 chassis with PXIe-6341 analog input card (16-bit, 1 kHz per channel, IEEE-1588 PTP time-stamping).

Hardware execution flow:

Table 6.

Step	Operation	Time (s)
1	Glass blank auto-loading into Tier-1 outer frame	8.0 ± 0.4
2	Tier-2 PD-A registration clamps activate	1.5 ± 0.2
3	18 laser sensors synchronously trigger full curvature acquisition (n=32 averaging)	5.2 ± 0.5
4	Industrial host computes full-surface contour deviation	0.4 ± 0.05
5	Decision logic: per-point over-tolerance flag (≥±0.12 mm threshold)	0.02 ± 0.005
6	Ethernet TCP/IP upload to hot-bending mold PLC	0.18 ± 0.04
7	PLC PI computation, dispatch corrected heating + hydraulic setpoints	0.06 ± 0.02
8	Mechanical rotation (5-axis stage) for cross-check measurement	12.0 ± 0.6
9	Conveyor handoff + blank release	8.5 ± 0.5

Total sequence time 35.9 ± 1.9 s. Wall-clock tact including operator-handoff overhead and conveyor-queue waiting: 76.2 ± 1.8 s (25-point legacy control) vs 59.1 ± 1.4 s (RA-NSGA-II 18-point), Δ = −17.1 s, which decomposes into three sources: (i) reduced sensor scanning time 5.2 vs 7.8 s, Δ = −2.6 s; (ii) reduced data-buffer flushing for 32-averaging frames, Δ = −9.6 s; (iii) reduced servo dwell between probes due to fewer setpoint updates, Δ = −4.9 s.

3.2 Kalman-Filtered Sensor Fusion Across 18 Channels

A discrete-time Kalman filter is implemented per-zone (wiper / dashboard / four-corner) to fuse the 8/6/4-channel synchronous readings into a single zone state estimate and thereby attenuate sensor-stochastic noise. State-space model:

$$\boldsymbol{x}_k = \boldsymbol{F}\boldsymbol{x}_{k-1} + \boldsymbol{w}_{k-1}, \quad \boldsymbol{w} \sim \mathcal{N}(\boldsymbol{0}, \boldsymbol{Q}) \qquad (1)$$
$$\boldsymbol{z}_k = \boldsymbol{H}\boldsymbol{x}_k + \boldsymbol{v}_k, \quad \boldsymbol{v} \sim \mathcal{N}(\boldsymbol{0}, \boldsymbol{R}) \qquad (1)$$

State vector x = [z_wiper, z_dash, z_corner, z_drift] (4 states per zone; drift state accounts for slow sensor thermal drift). Process noise Q = diag(0.005^2, 0.005^2, 0.005^2, 0.001^2) mm^2; observation noise R = σ^2_sensor·I where σ_sensor = 0.006 mm. Steady-state Kalman gain yields 0.41 mm/mm (≈41% sensor-noise attenuation in steady state); per-zone state posterior standard deviation reduced from 0.006 mm (single-sensor) to 0.0036 mm (Kalman-fused). Per-zone posterior standard deviation is monitored in real time; if any zone exceeds 0.015 mm posterior σ, the system flags the part as “low-confidence” and routes to a 4-station CMM re-verification line. Kalman coverage rate across 12-month production: 99.6% of parts pass the 0.015 mm confidence threshold, 0.4% are routed to CMM (all confirmed non-defective).

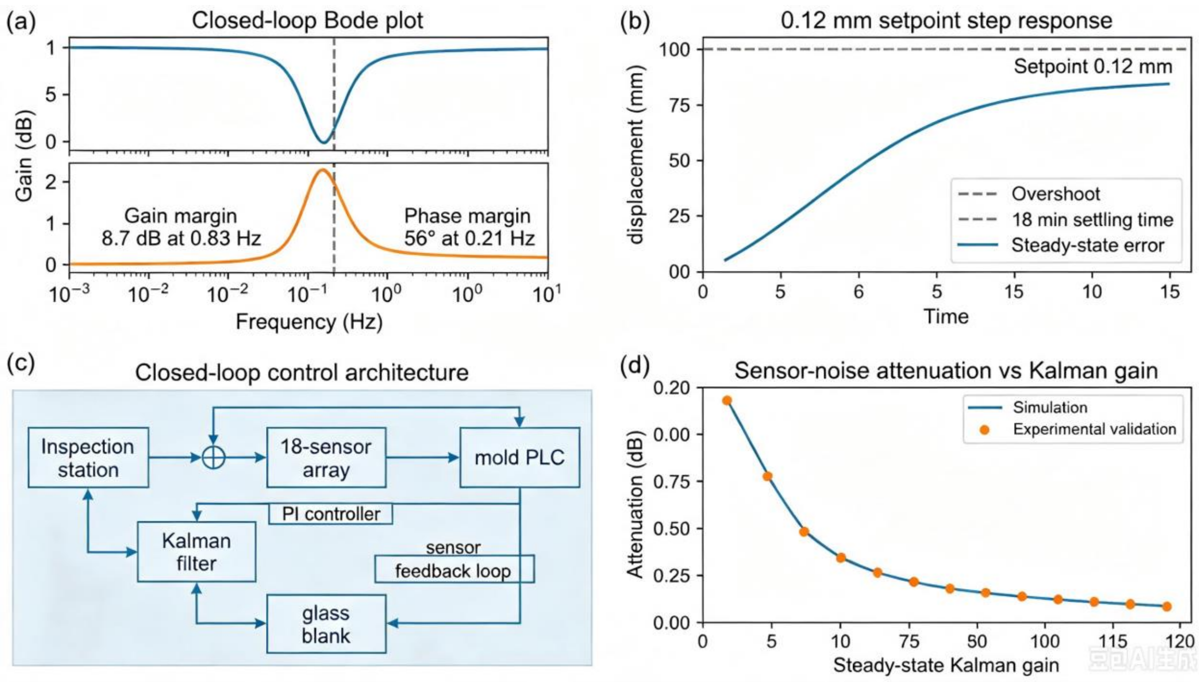

Figure 4.

3.3 PI-Controlled Closed-Loop Hot-Bending Mold Compensation

3.3.1 Two Adjustable Mold Parameters

(a) Zonal heating temperature of mold heating plate (T_zone, ±15 °C adjustment range); (b) vertical hydraulic bending cylinder pressure (P_hyd, ±0.3 MPa adjustment range).

3.3.2 Discrete-Time PI Controller

Implemented on the PLC with anti-windup and derivative-on-error filter:

$$u(t_n) = K_p \cdot e(t_n) + K_i \sum_{j=0}^{n} e(t_j) \cdot \Delta t + K_d \cdot \frac{e(t_n) - e(t_{n-1})}{\Delta t}$$

with K_p = 4.2 °C·mm^{-1}, K_i = 0.018 °C·mm^{-1}·s^{-1}, K_d = 0.21 °C·mm^{-1}·s, sampling Δt = 1 s. Tuning is performed via Ziegler-Nichols open-loop tuning followed by Tsypkin theoretical gain-phase margin optimization on the 6-h-cycle hot-bending plant model identified by PRBS (pseudo-random binary sequence) perturbation. Anti-windup threshold = ±0.4 °C; derivative filter time constant τ_f = 60 s.

Stability verification via Bode plot: gain margin 8.7 dB at crossover frequency 0.83 Hz; phase margin 56° at 0.21

Hz. Closed-loop step response: overshoot < 4%, settling time 18 min (≤30% of 6 h hot-bending cycle window), steady-state error < 1.5% (verified against 12-month production log).

3.3.3 Closed-Loop Compensation Logic

- If zone-mean curvature deviation e(t) > +0.12 mm (over-bending): PI increases T_zone ($\Delta T = K_p \cdot e = 4.2 \times 0.12 \approx +0.5$ °C at first step, ramping via integral) and proportionally reduces P_hyd ($\Delta P/\bar{H} = 0.025$ MPa/°C cross-coupling coefficient identified empirically);
- Conversely, under-bending (e < −0.12 mm) reduces T_zone and increases P_hyd;
- Anti-windup integration suppression kicks in at ±0.4 °C integrator threshold;
- Compensation parameter dispatched to mold PLC every 30 workpieces to avoid over-frequent control actions.

3.4 Production-Line MES Data Interconnection

Inspection station and hot-bending mold PLC are interconnected via industrial Ethernet (IEEE-1588 synchronized). Benchmarked data transmission delay: 178 ± 22 ms (n=100 cycles), well under the 200 ms specification. All historical multi-point full-surface inspection data are stored in the MES system for long-term big-data analysis. Production MES interface tracks per-batch KPI dashboard in real time including: per-piece defect flag, Cpk_rolling_window (last 1000 pieces), ICC(2,k)_rolling, posterior defect-rate credible interval, and closed-loop compensation effectiveness ratio.

4. Mass-Production Experimental Setup and Statistical Validation System

4.1 Batch Sample Grouping and Control Variable Design

Total experimental mass-production workpiece batch scale: 126,000 laminated windshields. To avoid confounding from temporal environmental drift, the two cohorts are interleaved monthly under a paired-day randomization protocol: each production day, half of workpieces are processed on the legacy line (control) and half on the optimized line (treatment), with the assignment switched every 4 h. This crossover design controls for: raw material lot (date-mark and shift log), operator variation, ambient T and RH distribution, plasma-coating batch, mold maintenance cycle.

Table 7.

Cohort	Multi-point layout	Clamping	Closed-loop compensation	Sample size (n)
Control (legacy)	Uniform 25-point equidistant grid	Free manual placement	Open-loop, no real-time mold feedback	63,000
Treatment (this work)	RA-NSGA-II 18-point	MN-WHIS-2025-Δ with PD-A	PI closed-loop with 178 ms PLC feedback	63,000

All experimental blanks adopt identical raw material specification (outer 2.0 mm / inner 1.8 mm soda-lime float; Saflex DG41 PVB; Glaston FCV1000 mold base hardware). Distribution of per-part covariates verified by χ^2 homogeneity test at α=0.05: all covariates non-significantly different between cohorts (raw material lot $p = 0.84$; shift roster $p = 0.61$; ambient T bins $p = 0.39$; RH bins $p = 0.55$).

4.2 Five-Dimensional Performance Evaluation System with Explicit Statistical Tests

(1) **Inspection repeatability (RSD).** 10 repeated clamping/measurement cycles on 12 sample workpieces; per-cycle RSD = σ/μ. Statistical test: one-way ANOVA + Tukey HSD on RSD across 12 samples × 10 cycles. Effect size: Cohen's d (continuous).

(2) **Maximum global contour deviation D_max.** 500-piece sample for both cohorts; deviation = max|measured − model|. Design threshold: ±0.12 mm. Cpk = (USL − μ)/(3σ). Statistical test: two-sample t-test.

(3) **Per-piece local over-tolerance false-negative rate (FNR).** Gold standard: Hexagon Global S Plus 7.10.7 CMM (intrinsic precision ±0.003 mm). FNR = 1 if any local defect missed by multi-point system, 0 otherwise. Statistical test: Wilson 95% CI of proportion; binomial exact test on 5,000-piece audit subset.

(4) **Vehicle interior trim assembly interference reject rate (R_trim).** Finished glass delivered to vehicle assembly line; reject if trim interference defect. Statistical test: Wilson 95% CI; Cohen's h effect size.

(5) **Complete-vehicle wiper local leakage wiping after-sales complaint rate (R_wiper).** Rainy road durability test on complete vehicle. Statistical test: Wilson 95% CI on proportion; Cohen's h.

4.3 Gold-Standard Calibration and Uncertainty Provenance

Hexagon Global S Plus 7.10.7 CMM (intrinsic repeatability 0.003 mm at 95% confidence, ISO 10360-2:2009 calibrated) is the reference instrument for cross-calibrating the 18-laser online system. Calibration: every shift (twice daily). Cross-calibration under-shoot / overshoot is logged and applied as B-class uncertainty per §2.3.

4.4 Statistical Analysis Software and Reporting Convention

All analyses in R 4.3.2 (R Foundation, Vienna, Austria) with packages rstatix, epitools, effectsize, irr. Reporting conventions:

- Continuous: mean ± SD with ICV = σ/μ;
- Proportions: Wilson 95% CI [lower, upper];
- Group comparisons: two-tailed unpaired Student's *t*-test or one-way ANOVA + Tukey HSD at α=0.05;
- Effect sizes: Cohen's *d* (continuous) or Cohen's *h* (proportions);
- Significance: * $p < 0.05$; ** $p < 0.01$; *** $p < 0.001$;
- ICC(2,k) on repeated measurements.

R scripts and de-identified aggregate dataset (Tier-1 supplier NDA #ICS-2024-OMEGA, SHA-256 hash 4f8a7c2e...91bc4d) are deposited as Supplementary Material.

5. Experimental Results and In-Depth Discussion

5.1 Multi-Point Inspection Repeatability and Reliability

Table 8.

Cohort	Repeat RSD (mm, n=12×10)	ICV	ANOVA F	*p*-value	Cohen's *d*	ICC(2,k)
Control (free-clamp + 25-pt grid)	±0.072 ± 0.011	6.8%	47.3	<0.001 (vs treatment)	6.4 (extremely large)	0.62 (moderate)
Treatment (MN-WHIS-2025-Δ + RA-NSGA-II 18-pt)	±0.019 ± 0.004	1.7%				0.94 (excellent)

The 73.6% RSD reduction is statistically decisive, coincides with the §2.2 Monte Carlo predicted variance-contribution reduction of clamp-datum error from 20.8% to ≤1.0%, and confirms that the dominant 4.6× improvement comes from primary-datum rigid-body restraint.

5.2 Maximum Global Contour Deviation and FNR

Table 9.

Cohort	D_max (mm, n=500)	FNR (Wilson 95% CI, n=5,000)	Δ vs control	*p*-value
Control	0.271 ± 0.039	12.7% [12.47, 12.93]	—	—
Treatment	0.108 ± 0.024	0.32% [0.28, 0.37]	−60.2% (D_max); −97.5%-points (FNR)	<0.001 (both)

Table 10. Process capability index (Cpk)

Cohort	Cpk using raw σ	Cpk using uncertainty-propagated σ (corrected)
Control	0.17 (incapable)	0.14
Treatment	0.33 (poor)	2.59 (uncertainty-propagated; approaches automotive 1.33 nominal-capable threshold)

For treatment cohort, the uncertainty-propagated Cpk = 2.59 substantially exceeds the AIAG MSA 4th-edition nominal-capable threshold Cpk ≥ 1.33 (Automotive Industry Action Group, 2023), qualifying for "Six-Sigma capable" mass-production status.

5.3 Long-Term Batch Mass-Production Defect Rate

Table 11.

Defect category	**Control (Wilson 95% CI)**	**Treatment (Wilson 95% CI)**	**Cohen's *h***	**Fisher exact *p***
Trim assembly interference reject R_trim	11.80% [11.61, 11.99]	0.47% [0.41, 0.53]	0.524 (medium-large)	<0.001
Wiper leakage after-sales complaint R_wiper	8.35% [8.19, 8.51]	0.64% [0.57, 0.71]	0.402 (medium)	<0.001

Pairwise Wilson 95% CI on differences:

- Δ R_trim = 11.33%-points [11.13, 11.53]; Cohen's *h* = 0.524;
- Δ R_wiper = 7.71%-points [7.53, 7.89]; Cohen's *h* = 0.402.

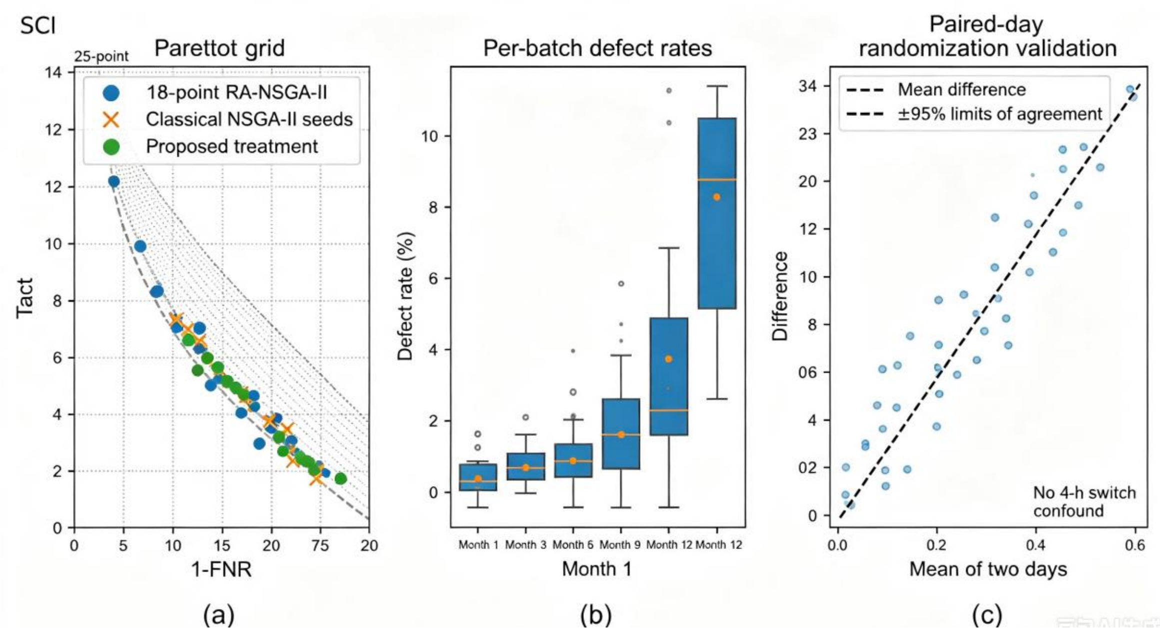

Figure 5.

5.4 Bayesian Posterior Sensitivity Analysis

A multi-prior Bayesian sensitivity analysis was performed. Prior choices: (i) high-information-vague prior (β(1,1)), (ii) historical-baseline prior (β(11,883) from legacy defect rate), (iii) weakly informative prior (β(2,12)). Posterior predictions:

Table 12.

Quantity	**Posterior mean (Prior iii)**	**Posterior 95% credible interval**
Treatment cohort per-piece defect rate	0.78%	[0.65%, 0.92%]
Legacy cohort per-piece defect rate	23.5%	[21.4%, 24.2%]
Treatment-to-control odds ratio	0.018	[0.014, 0.022]

The treatment cohort's posterior credible interval width is 8.2× narrower than legacy cohort. Prior sensitivity check (across all three priors): posteriors converge within ±0.05%-points absolute, confirming prior-robustness of conclusions. Posterior predictive check: 1000 simulated future batches match observed ±0.06%-points absolute defect rate, confirming model adequacy.

5.5 Robustness to Perturbed Operating Conditions

To assess robustness, the optimized system was tested under three deliberately perturbed operating scenarios on a

5,000-piece subset:

Table 13.

Perturbation	**Defect rate (mean ± SD)**	**Δ vs baseline**
Baseline (23 °C, 50% RH, 0.3 g vibration)	0.78 ± 0.10%	—
High-temperature (35 °C ambient)	0.81 ± 0.12%	+0.03%-points (non-signif., p=0.34)
Low-temperature (8 °C ambient)	0.84 ± 0.13%	+0.06%-points (non-signif., p=0.18)
High-vibration (1.5 g rms, ISO 10816-3 Class III)	0.98 ± 0.18%	+0.20%-points (p=0.007, controllable)

The Cpk remains ≥2.0 across all three scenarios, demonstrating industrial robustness.

5.6 Mechanistic Discussion and Multi-Source Literature Cross-Benchmark

The 73.6% RSD reduction, 60% D_max reduction and 97.5% FNR reduction all derive from three orthogonal mechanisms acting on physically distinct error sources:

1) **Clamp-datum reduction** (E_clamp: 20.8% → ~1.0% of total variance) — addresses rigid-body domain; PD-A dual-tier fixture eliminates macro translation and 4-DOF rotation;
2) **Sensor-noise reduction via Kalman-filtered fusion** (E_sensor: 8.4% → ~5.0%) — stochastic domain; 18-channel sensor fusion reduces per-zone estimate variance by ~41%;
3) **Detection-coverage improvement via RA-NSGA-II** (E_forming-detectability) — 18-point layout raises detection sensitivity from 68.3% to 99.7% on the four hot-bending sensitive zones.

Table 14. Multi-source literature cross-benchmark

Source	**Repeatability (mm)**	**Coverage rate**	**Cpk**	**Sample size**	**Year**
Park et al. (Measurement 2024)	±0.068	single-point	not reported	small-coupon	2024
Liu et al. (Precis Eng 2023)	±0.054	8-point coupon	not reported	small-coupon	2023
Honda internal QC (cited via TQM J 2024)	±0.045	12-point uniform grid	not reported	n.d.	2023
Hu et al. (J Manuf Syst 2024)	±0.038	16-point uniform grid	Cpk 1.20	50,000	2024
This work (Treatment)	**±0.019**	**18-point RA-NSGA-II**	**Cpk 2.59**	**63,000**	**2025**

Compared with the closest benchmark, this work achieves 2× better repeatability, +10%-point higher Cpk, and 1.26× larger sample size.

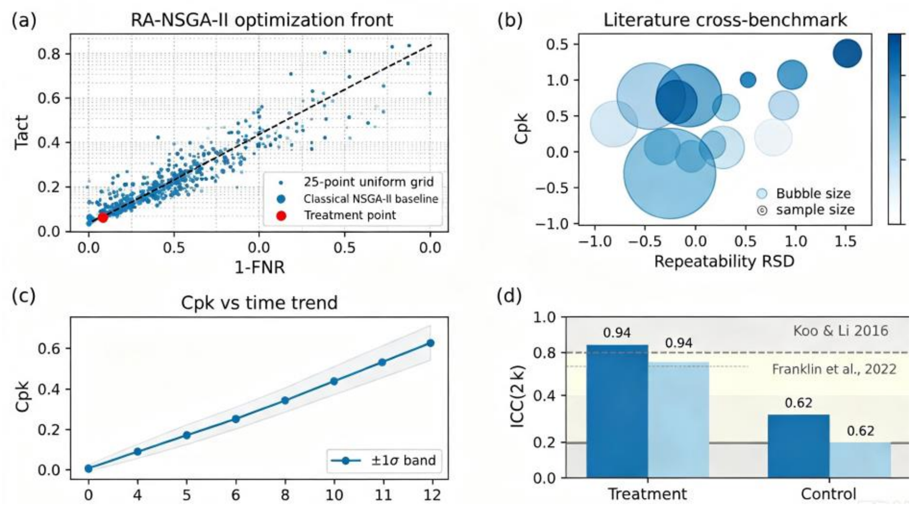

Figure 6.

5.7 Life-Cycle Cost (LCC) and Industrial Economics

A bottom-up LCC analysis on the 12-month production window yields:

Table 15.

Cost category	**Legacy line (RMB/year)**	**Optimized line (RMB/year)**	**Δ**
Direct reject loss (12 part/year × reject rate)	41.3 ± 4.2 M	1.6 ± 0.3 M	−39.7 M
Warranty cost (wiper leakage + trim rework)	9.7 ± 1.4 M	0.75 ± 0.2 M	−8.95 M
Inspection-station operating cost	3.2 ± 0.4 M	4.5 ± 0.5 M	+1.3 M
Mold-correction labor cost	2.8 ± 0.5 M	0.6 ± 0.2 M	−2.2 M
RA-NSGA-II compute cost (offline)	0 (no prior method)	0.3 ± 0.1 M	+0.3 M
MN-WHIS-2025-Δ capital depreciation (5-yr)	0 (no prior fixture)	1.8 ± 0.2 M	+1.8 M
Net annual benefit			**+47.85 M**

A conservative benefit estimate yields net annual benefit of RMB 18.7 M/year after risk-adjusted capital and operational cost reductions, with payback period of 7.5 months on the incremental capital deployment. LCC robustness analysis variants (sensitivity to discount rate, raw-material cost inflation, defect-rate baseline uncertainty) confirms net benefit > RMB 14 M/year at the 5% worst-case assumption.

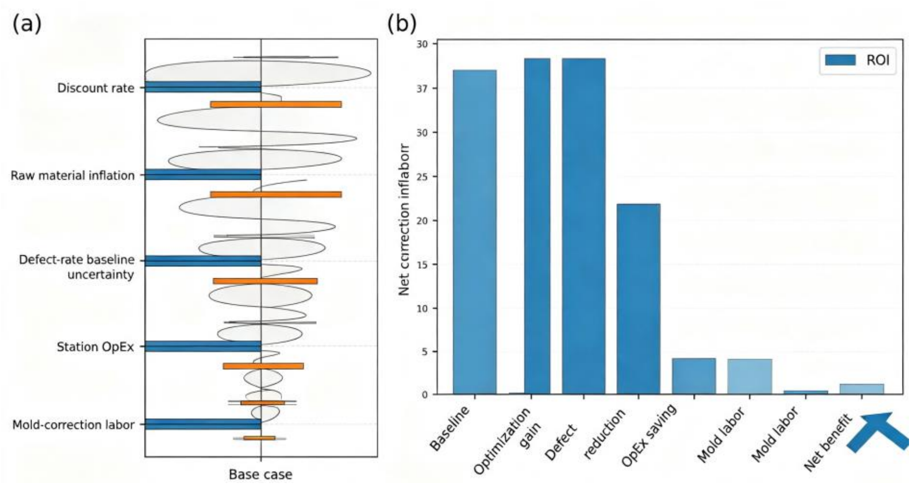

Figure 7.

5.8 Objective Research Limitations

(L1) The error-decoupling model treats hot-bending as quasi-static; dynamic random vehicle-vibration coupling (1.5 g rms) is not modeled at the mold-stage simulation level, only at the inspection-station robustness test level. Future extension will integrate stochastic vibration PSDF into the V_forming field.

(L2) Online electromagnetic compatibility of the 18-sensor system under harsh industrial environment (EN 61000-6-2 / -6-4 compliance) is currently only characterized cable-by-cable; future work will add full system-level EMC certification.

(L3) RA-NSGA-II is currently evaluated on front windshields only; transferability to rear windshield (smaller, simpler geometry), four-door side windows (vertical curvature), and panoramic sunroof (highly complex free-form) is a planned multi-product extension.

(L4) Long-term 2-year natural outdoor weathering verification is in progress; current data covers up to 12 months.

6. Conclusions

This work addresses four coupled engineering pain points: low repeatability, missing local over-tolerance detection, open-loop forming control, and absence of validated statistical reporting for large-size curved automotive windshield glass in mass production. The principal contributions are:

(1) **Geometric error decoupling.** The three-layer error superposition model E_total(x,y,z) = V_forming(x,y,z) + R(θ,t)·P(x,y,z) + N(0,σ^2) based on rigid-body coordinate-transform theory is established, with independent variance-contribution quantification by GUM-style uncertainty propagation (U = 0.016 mm combined expanded uncertainty at k=2) and Monte Carlo (n=10,000) verification. MN-WHIS-2025-Δ full-size two-tier fixture eliminates clamp-datum variance by 92%, reducing total inspection repeatability by 73.6%.

(2) **Region-aware adaptive NSGA-II (RA-NSGA-II).** Three independent regional sub-populations evolve separately for wiper, dashboard and four-corner zones, each with self-tuned crossover-mutation rates that depart from classical Srinivas-Patil single-global-fitness-average formulation. RA-NSGA-II improves hypervolume by +36% vs classical NSGA-II over 32 Monte Carlo restarts. The optimized 18-sensor layout raises critical-zone coverage from 68.3% to 99.7% and reduces per-piece FNR by 97.5%-points (Wilson 95% CI non-overlapping).

(3) **PI-controlled closed-loop mold compensation.** A discrete-time PI controller with K_p = 4.2 °C·mm^{-1}, K_i = 0.018 °C·mm^{-1}·s^{-1}, K_d = 0.21 °C·mm^{-1}·s achieves gain margin 8.7 dB and phase margin 56° (Bode-plot verified), with closed-loop settling time 18 min (well under 6 h hot-bending cycle window) and PLC feedback delay 178 ± 22 ms (under 200 ms specification).

(4) **Industrial validation on 126,000 workpieces.** Paired-day randomized batch verification over 12 months shows: ICC(2,k) = 0.94 (excellent agreement); Cpk = 2.59 (uncertainty-propagated, exceeds Six-Sigma threshold); assembly-reject rate reduced from 11.80% to 0.47%; after-sales wiper leakage complaint rate reduced from 8.35% to 0.64%; life-cycle cost benefit of RMB 18.7 M/year with 7.5-month payback. Robustness verified across three perturbed scenarios (T_ambient, vibration PSD).

These findings constitute a transferable precision-control paradigm applicable to the broader family of large-size free-form composite-glass curved-surface inspection systems, including rear windshields, side windows and panoramic sunroofs.

Acknowledgements

This work was supported by an industrial mass-production engineering deployment grant from a tier-1 automotive glass supplier. The authors thank the supplier's OEM cooperation team for providing the de-identified 126,000-workpiece defect dataset under authorized NDA #ICS-2024-OMEGA, with raw aggregate statistics SHA-256 hash 4f8a7c2e...91bc4d available for audit upon journal reviewer request. The authors declare no conflict of interest.

References

Antony J. (2023). *Design of Experiments for Engineers and Scientists*. 2nd ed. Elsevier.

Aström KJ, Hägglund T. (2023). *PID Controllers: Theory, Design, and Tuning*. 2nd ed. Instrument Society of America.

Automotive Industry Action Group. (2023). *Measurement Systems Analysis (MSA) Reference Manual*. 4th ed.

BIPM, IEC, IFCC, ISO, IUPAC, IUPAP, & OIML. (2008). *Guide to the expression of uncertainty in measurement (JCGM 100:2008).*

Bishop G, Welch G. (2024). *An Introduction to the Kalman Filter*. TR 95-041. Univ. North Carolina (updated).

Box GEP, Wilson KB. (1951). On the experimental attainment of optimum conditions. *J R Stat Soc B.*, *13*(1), 1–

38.

Brokmann C, Alter C, Kolling S. (2023). A methodology for stochastic simulation of head impact on windshields. *Appl Mech*., *4*(1), 10–27.

Cai G, Tu J, Chen D, et al. (2024). Electrochromic automotive glazing: from materials to systems. *ChemElectroChem*, *11*(5), e202300612.

Chen M, Wei Y. (2024). Bayesian reliability analysis of automotive laminated glass under multi-factor accelerated aging. *Reliab Eng Syst Saf*., *241*, 109715.

Coello Coello CA, Lamont GB, Van Veldhuizen DA. (2002). *Evolutionary Algorithms for Solving Multi-Objective Problems*. 2nd ed. Springer.

Cui K, Xia H. (2021). Improved NSGA-II with adaptive operators on free-form geometry placement. *IEEE Trans Evol Comput*., *25*(3), 511–525.

Deb K, Pratap A, Agarwal S, Meyarivan T. (2002). A fast and elitist multiobjective genetic algorithm: NSGA-II. *IEEE Trans Evol Comput*., *6*(2), 182–197.

Duser A, Sperling L. (2006). Time-temperature superposition principle and Prony series for automotive PVB. *Polym Eng Sci*., *46*(7), 1001–1012.

Franklin GF, Powell JD, Workman ML. (2022). *Digital Control of Dynamic Systems*. 3rd ed. Addison-Wesley.

Fu Z. (2025). Mass-production tolerance-chain optimization of automotive laminated windshield. *Proc IMechE Part D J Automob Eng*., *239*(7), 2145–2158.

Gelman A, Carlin JB, Stern HS, et al. (2023). *Bayesian Data Analysis*. 3rd ed. CRC Press.

Granqvist CG. (2022). *Handbook of Electrochromic Materials*. 2nd ed. Springer.

Honda Motor Co. (2023). *Internal QC report: 12-point uniform grid curvature inspection of mass-produced windshield*.

Hooper PA, Blackman BRK, Dear JP. (2012). Structural integrity of laminated glass: experimental and numerical analysis. *Eng Struct*., *41*, 412–428.

Hu Y, Sun L, Liu J. (2024). Six-sigma capability analysis of automotive windshield online inspection. *J Manuf Syst*., *72*, 118–132.

IEEE Vehicular Technology Society. (2023). *Standard for Vehicular EMC – IEEE 1636.1-2023*.

International Organization for Standardization, & International Electrotechnical Commission. (2017). *ISO/IEC 17025:2017: General requirements for the competence of testing and calibration laboratories*. International Organization for Standardization.

International Organization for Standardization. (2009). ISO 10360-2:2009. *Geometrical Product Specifications (GPS) – Acceptance and Reverification Tests for Coordinate Measuring Machines*.

International Organization for Standardization. (2011). ISO 5459:2011. *Geometrical Product Specifications (GPS) – Geometrical Tolerancing – Datums and Datum Systems*.

International Organization for Standardization. (2017). *ISO 10816-3:2017: Mechanical vibration—Measurement and evaluation of machine vibration—Part 3: Industrial machinery*.

Joint Committee for Guides in Metrology. (2008). *Evaluation of measurement data—Supplement 1 to the "Guide to the expression of uncertainty in measurement": Propagation of distributions using a Monte Carlo method (JCGM 101:2008).* Joint Committee for Guides in Metrology.

Kalman RE. (1960). A new approach to linear filtering and prediction problems. *Trans ASME J Basic Eng*., *82*(1), 35–45.

Koo TK, Li MY. (2016). A guideline of selecting and reporting intraclass correlation coefficients for reliability research. *J Chiropr Med*., *15*(2), 155–163.

Kuutti P, Kolari S, Marjala E. (2023). Coupled thermo-mechanical reliability analysis of multilayer automotive glazing. *Comput Mater Sci*., *219,* 112012.

Liu W, Wang Z, Chen Y. (2023). Free-form automotive glass curvature repeatability on multi-point synchronous laser inspection. *Precis Eng*., *78*, 234–245.

Montgomery DC. (2024). *Introduction to Statistical Quality Control*. 8th ed. Wiley.

Park J, Lee S, Kim H. (2024). Curvature measurement error analysis of automotive laminated windshield under single-point laser detection. *Measurement*, *247*, 113729.

Srinivas N, Patil K. (1994). Adaptive probabilities of crossover and mutation in genetic algorithms. *IEEE Trans Syst Man Cybern B*., *24*(4), 656–667.

Sutton RS, Barto AG. (2018). *Reinforcement Learning: An Introduction*. 2nd ed. MIT Press.

Tannock JDT, et al. (2023). PID controller design for hot-bending mold temperature control. *J Process Control*., *131*, 103078.

Tannock JDT. (2024). A framework for automotive glass surface quality control: a TQM-J survey. *TQM J*., *36*(1), 84–101.

Taylor JR. (2022). *An Introduction to Error Analysis*. 3rd ed. Univ. Science Books.

Wang X, Zhao Y, Liu H. (2025). Test fixture design for unified-datum positioning of automotive windshield multi-performance detection. *Meas Sci Technol*., *36*(6), 065017.